inorganics

MDPI

Article

Mechanism of High-Rate Cycling Stability of Anthraquinone Cathode for Aqueous Zinc-Ion Batteries

Qiujie Chen [1,2], Xiaoxu Lai [1,2], Wenlan Chen [1,2,3], Chi Chen [1,2], Houzhao Wan [4,]* and Dan Sun [1,2,]*

[1] CAS Key Laboratory of Design and Assembly of Functional Nanostructures and Fujian Provincial Key Laboratory of Nanomaterials, Fujian Institute of Research on the Structure of Matter, Chinese Academy of Sciences, Fuzhou 350002, China; xmchenqiujie@fjirsm.ac.cn (Q.C.); xmlaixiaoxu@fjirsm.ac.cn (X.L.); xmchenwenlan@fjirsm.ac.cn (W.C.); xmchenchi@fjirsm.ac.cn (C.C.)
[2] Xiamen Key Laboratory of Rare Earth Photoelectric Functional Materials, Xiamen Institute of Rare Earth Materials, Haixi Institute, Chinese Academy of Sciences, Xiamen 361021, China
[3] College of Chemistry and Materials, Fujian Normal University, Fuzhou 350007, China
[4] Hubei Key Laboratory of Ferro & Piezoelectric Materials and Devices, School of Microelectronics and Faculty of Physics and Electronic Science, Hubei University, Wuhan 430062, China
* Correspondence: houzhaow@hubu.edu.cn (H.W.); xmsundan@fjirsm.ac.cn (D.S.)

Abstract: Aqueous zinc-ion batteries (ZIBs) are an appealing rechargeable battery technology for next-generation energy storage devices, known for their low cost and high safety. Among the promising cathode materials used for aqueous ZIBs, anthraquinone (AQ) stands out due to its high theoretical specific capacity, low cost, and environmental friendliness. In this study, we investigate the cyclic stability of AQ in aqueous ZIBs. We demonstrate that AQ exhibits a good capacity retention at a high current density even after 1000 charge–discharge cycles, while more obvious capacity fading is observed at a low current density. Density functional theory calculations reveal that the mechanism of the rapid capacity fading under a low current density is due to the significant structural deformation of AQ crystal during Zn insertion into the AQ bulk. Furthermore, the energy barrier of Zn ions that diffuse into the AQ bulk is much higher than the diffuse on the AQ surface, leading to an irreversible Zn insertion. However, under a high current density, Zn ions prefer to adsorb and diffuse on the AQ surface without bulk insertion and structural deformation, rending a higher cycling stability. These insights into the factors influencing the cycling stability of AQ-based electrodes offer a guidance to improve their performance for practical applications.

Keywords: organic cathode; aqueous zinc-ion batteries; diffusion mechanism; density functional theory calculations

check for updates

Citation: Chen, Q.; Lai, X.; Chen, W.; Chen, C.; Wan, H.; Sun, D. Mechanism of High-Rate Cycling Stability of Anthraquinone Cathode for Aqueous Zinc-Ion Batteries. *Inorganics* **2023**, *11*, 271. https://doi.org/10.3390/inorganics11070271

Academic Editor: Christian Julien

Received: 27 April 2023
Revised: 19 June 2023
Accepted: 19 June 2023
Published: 25 June 2023

1. Introduction

Zn-ion batteries (ZIBs) are emerging as promising advanced rechargeable batteries due to their excellent properties, including a high theoretical capacity, good rate performance, low cost, environmental friendliness, and high safety [1–4]. Among various multivalent chemistries, zinc stands out as the optimal choice for a reversible anode in aqueous electrolytes, owing to its inherent stability and relatively high overpotential for hydrogen evolution [5,6]. The combination of aqueous electrolytes with zinc anodes provides safety advantages. However, the development of cathode materials is crucial to further enhance the performance of aqueous ZIBs [7–9]. Present cathode materials for aqueous ZIBs, such as metal oxides, polyanionic olivine-based phosphates, and so on [10,11], face challenges including sluggish kinetics, low efficiency, and unstable cycling [12]. Additionally, many of these cathode materials involve toxic or environmentally harmful elements. Overcoming these obstacles necessitates the discovery of sustainable cathodes that exhibit a long cycling stability, high energy density, and large power density. Organic materials, especially anthraquinone (AQ) and its derivatives, have garnered significant interests as promising

Inorganics **2023**, *11*, 271. https://doi.org/10.3390/inorganics11070271 https://www.mdpi.com/journal/inorganics

cathode materials owing to their large theoretical specific capacity, low cost, and inherent eco-efficiency [13–16]. Additionally, the redox potential of AQ is compatible with the electrochemical window of most battery electrolytes [17,18]. The large conjugation between the carbonyl group and aromatic frame of AQ, as well as its aromatic ring structure, contribute to its high theoretical capacity of 257 mAh/g, making it an extensively researched material in various batteries [19–21]. However, the poor cycling stability of AQ limits its further use in ZIBs [22]. The poor cycling stability of electrodes based on low-molecular-weight organic active materials is mostly attributed to their dissolution or leaching into the electrolyte [23–25]. To address this issue, researchers replaced the organic solvent electrolyte with water, which reduces the solubility of AQ active materials due to its low solubility in water [26]. With the potential high energy density, AQ can serve as a promising cathode candidate for aqueous ZIBs.

To investigate the cycling performance of AQ for aqueous ZIBs, we conducted electrochemical experiments with AQ cathodes for aqueous ZIBs subjected to over 1000 charge−discharge cycles. Our experiment results revealed that the capacity retention rate is good at a high current density (after 1000 cycles with a capacity fading rate of about 0.03% per cycle), while a rapid decrease in the capacity at a low current density is observed (after 1000 cycles with a capacity fading rate of about 0.08% per cycle). This suggests that AQ has the potential to be an effective electrode material in practical applications where a high-power output is required. Nonetheless, further investigations are needed to understand the underlying reasons for the decrease in the AQ electrode capacity at a low current density, which is crucial for the development of high-performance ZIBs.

This work aims to investigate the rapid capacity decline of AQ cathodes in ZIBs under a low current density by combining experimental and theoretical calculation methods. The crystal structure and morphology of the AQ electrode before and after Zn ion insertion/de-insertion were studied to analyze the reason for the capacity attenuation of AQ electrodes from a crystallographic perspective. The diffusion behavior of Zn ions in AQ electrodes was studied using the climbing image nudged elastic band (CI-NEB) method. The diffusion mechanism of Zn ions in AQ electrodes was further clarified through the analysis of the diffusion path and energy barrier.

2. Results and Discussion

The XRD patterns of AQ powders and AQ/ketjen black (KB) composite are shown in Figure 1a. Both the characteristic peaks of the AQ powders and AQ/KB composite are well indexed to the standard card JCPDS No. 28-2002. This phenomenon could be explained by the fact that AQ is combined with KB via van der Waals force, and the amorphous KB has a negligible effect on the crystal structure of AQ. In addition, even though the AQ/KB composite was manufactured by ball milling, the crystal structure of the AQ/KB composite is consistent with AQ, implying that ball milling would not destroy the structure of pristine AQ.

The as-prepared AQ and AQ/KB composite morphologies were observed via TEM, as shown in Figure 1b,c, respectively. In Figure 1b, the size of a pristine nanorod-like AQ is about 400 nm in diameter, while the AQ in the AQ/KB composite exhibits a reduced size of around 200 nm caused by ball milling, which is uniformly covered by abundant KB nanoparticles (Figure 1c). KB as a conductive agent that enhances the intrinsically inferior electronic conductivity of AQ, thus improving the electrochemical performance.

To evaluate the electrochemical performance of ball-milled AQ, the cyclic voltammetry (CV) and galvanostatic charge/discharge tests of cells using zinc foil as an anode and AQ electrode as a cathode were carried out. Figure 2a presents the CV curves of the cell of AQ at a scan rate of 0.1 mV/s, which show two set peaks at 0.44–0.50 V and 0.63–0.65 V, corresponding to the redox reaction of the carbonyl group (C=O) of AQ, along with the coordination/incoordination of Zn^{2+}, respectively. Figure 2b displays the charge–discharge curves under a 200 mA/g current density of AQ at the 1st, 2nd, 50th, and 100th cycles, respectively. Two flat and long voltage plateaus are consistent with the redox peaks of the

CV curves. The discharge capacities from the 1st to 100th cycle are 219 and 117 mAh/g, respectively, indicating a low cycling stability under the current density of 200 mA/g. Figure 2c illustrates the charge–discharge curves of AQ at the current density of 4000 mA/g for the 1st, 2nd, 50th, 100th, and 200th cycles. The discharge capacities for the 50th, 100th, and 200th cycles are 140, 131, and 124 mAh/g, respectively, with the 1st being an exception at 81 mAh/g. These results indicate a high level of cycling stability under the current density of 4000 mA/g.

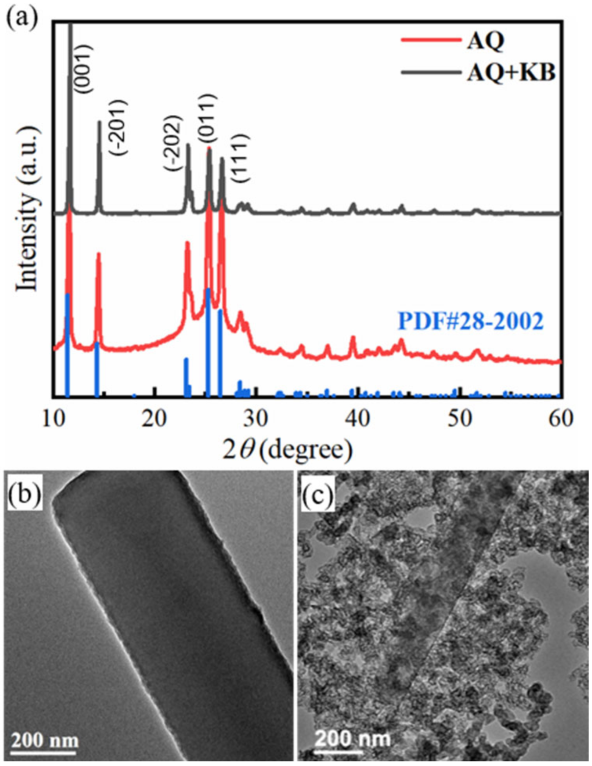

Figure 1. (**a**) XRD patterns of AQ (red) and AQ/KB composite (black). High-resolution TEM of (**b**) AQ and (**c**) AQ/KB composite after ball milling.

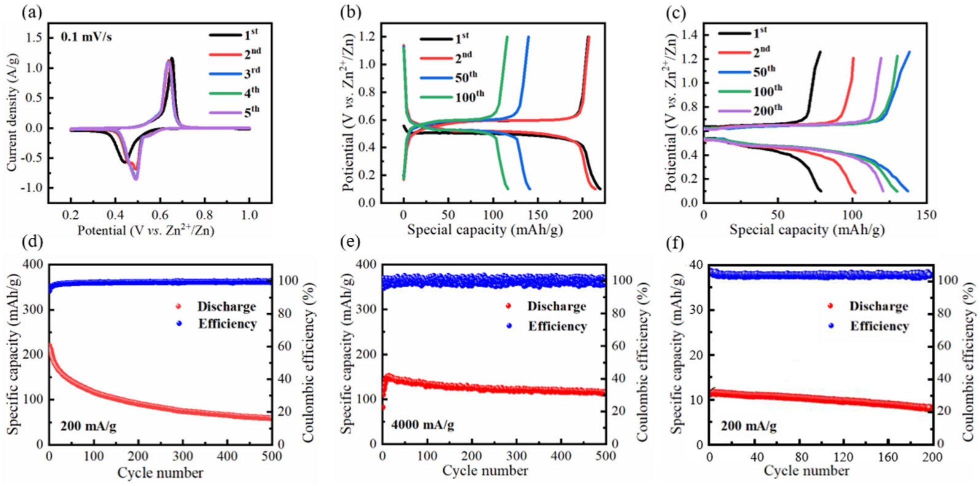

Figure 2. CV curves of AQ at a scan rate of 0.1 mV/s from 0.2 to 1.0 V (**a**), galvanostatic charge−discharge profiles of AQ at 1st, 2nd, 50th, and 100th cycles under (**b**) 200 mA/g current density and (**c**) 4000 mA/g current density. Cycling performance of AQ at (**d**) 200 mA/g and (**e**) 4000 mA/g. (**f**) Cycling performance of KB at 200 mA/g.

To further investigate the influence of the current density on the cycling performance of AQ, the long-term cycling was tested at the current densities of 200 and 4000 mA/g, respectively (Figure 2d,e). The discharge capacity of AQ drops from 219 to 40 mAh/g at 200 mA/g after 1000 cycles, with a capacity fading rate of about 0.08% per cycle. However, under a high current density of 4000 mA/g, the discharge capacity of AQ becomes steady after an eleven-cycle activation and decreases from the maximum value of 151 to 99 mAh/g after 1000 cycles, with a capacity fading rate of about 0.03% per cycle, which is lower than that at a current density of 200 mA/g. It suggests that AQ exhibits good capacity retention at a high current density, while capacity fading is more pronounced at a low current density.

In order to establish a control for our experiments, we conducted a capacity test on a pure KB electrode, which we refer to as the "blank" electrode. This electrode consisted solely of KB without the inclusion of AQ, as outlined in the methodology. Figure 2f presents the results of this test, showing an initial capacity of only 11 mAh/g for the pure KB electrode. This value is significantly lower when compared to the capacity demonstrated by the AQ + KB electrode. These findings provide conclusive evidence that the presence of AQ plays a primary role in influencing the overall capacity, rather than KB. Therefore, it can be concluded that the addition of KB to AQ has a negligible impact on the overall capacity, as observed in our experimental results.

To figure out the mechanism of a better cycling performance at a high current density, the first-principal calculations based on the density functional theory (DFT) were performed. The crystal structures of AQ were analyzed, revealing that monoclinic AQ consists of a conjugated aromatic compound with two carbonyl groups, belonging to a space group of $P2_1/c$. The shortest intermolecular distance within the AQ crystal lattice was found to be 3.942 Å along the b-axis. This compact structure, facilitated by the van der Waals force between the AQ molecules, creates ample space for Zn^{2+} diffusion. The lattice parameters (7.81 Å, 3.92 Å, and 15.66 Å) of the AQ crystal are in agreement with the reported value in [27]. To simulate the Zn insertion process into the AQ electrode, we expanded the AQ unit cell to a $2 \times 3 \times 1$ supercell with the lattice parameters of 15.63 Å, 11.75 Å, and 15.66 Å, respectively. We identified four possible insertion sites for Zn atoms in AQ bulk (sites A, B, C, and D), as illustrated in Figure 3. The binding energy (eV/Zn atom) was determined as the difference between the total energy of the Zn atom adsorbed on the AQ bulk and the sum of the total energy of the isolated Zn atom (belonging to Zn metal crystal, with a hexagonal close-packed structure and a lattice constant of 2.62 Å and 4.84 Å) and the isolated $2 \times 3 \times 1$ AQ supercell. The binding energies of the Zn atoms at four different adsorption sites are listed in Table 1. It is evident that the binding energy of Zn only at the C site exhibits a negative value of -0.95 eV, whereas at the other three sites, the binding energies are positive values no smaller than 1.16 eV. A positive binding energy signifies an endothermic reaction, indicating the low likelihood of Zn existing stably at these sites. This observation suggests that Zn atoms are more likely to be adsorbed at the C site of the AQ bulk.

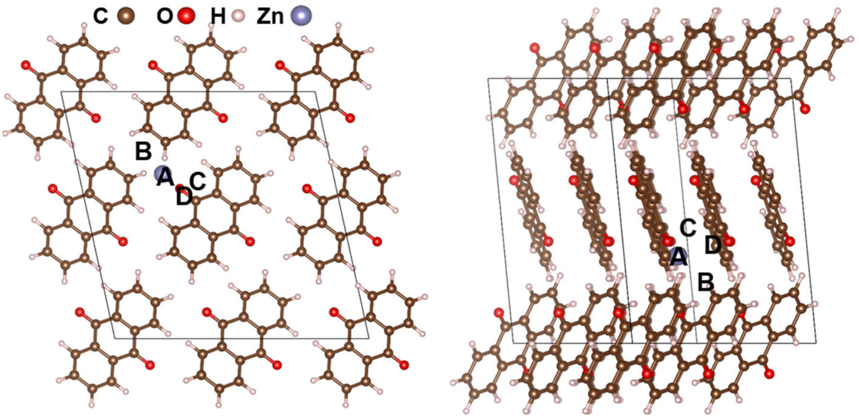

Figure 3. Top and side view of insertion sites of Zn in AQ bulk.

Table 1. The binding energies of Zn in AQ bulk.

	A Site	**B Site**	**C Site**	**D Site**
Binding energy (eV)	1.81	1.16	−0.95	1.16

The atomic structures of pristine and Zn (C site)-inserted AQ presented in Figure 4a,b show that the Zn atom bonded to two O atoms, resulting in the reduction in the carbonyl group (C=O double bond) in the AQ molecule and its subsequent conversion into a carbon–oxygen single bond. Additionally, we employed a non-in situ Fourier transform infrared spectroscopy (FTIR) to investigate the original structure of the AQ electrode and its first discharge state, as shown in Figure 4c. We detected a strong characteristic band at 1678 cm^{-1} in the original AQ structure, which is associated with the stretching vibration of the C=O group. After the first discharge, the carbonyl stretching signal decreased, indicating a reduction in the number of carbonyl groups in the AQ molecule. Based on the theoretical calculations and experimental discoveries, it can be concluded that after discharge, the carbonyl groups (C=O) in AQ transform into carbon–oxygen single bonds, coordinating with Zn ions to form a reduced state, where the carbonyl groups act as the center of the redox reactions.

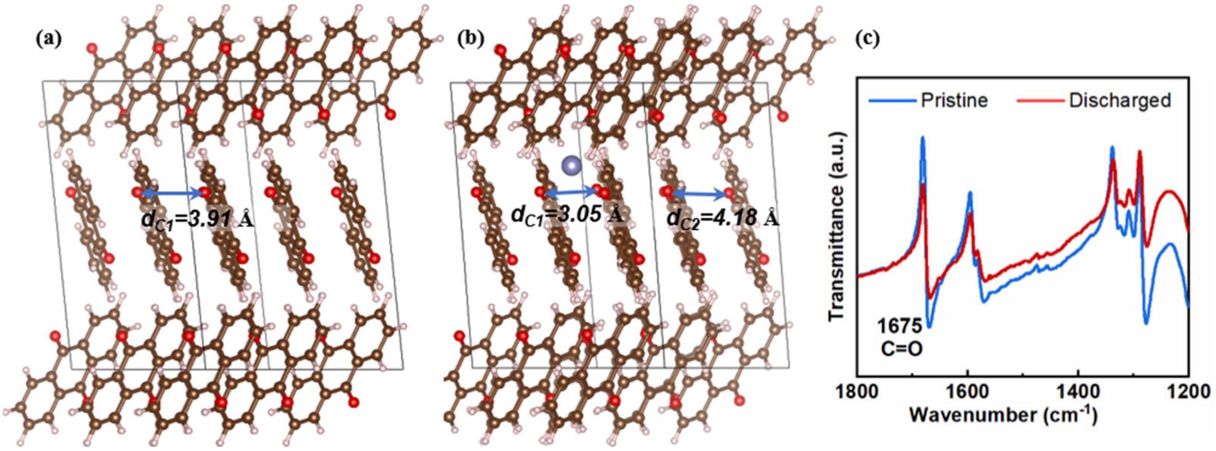

Figure 4. Optimized geometries of (**a**) pristine AQ supercell and (**b**) Zn-inserted AQ supercell; (**c**) FTIR spectra of AQ electrode before and after the 1st discharge.

To gain insight into the Zn atom insertion and de-insertion process in the AQ electrodes, we analyzed the structural change during the Zn insertion into the C site of the AQ bulk, as shown in Figure 4a,b and listed in Table 2. Table 2 shows a significant change in the lattice constants of AQ before and after the insertion of Zn, with the b-axis direction showing the most significant change, decreasing by approximately 3.66%. The c-axis also decreased, though slightly less than the b-axis, by approximately 1.28%. As a result, the volume of AQ decreased from its original value of 2808.02 $Å^3$ to 2654.74 $Å^3$, corresponding to a decrease of 5.46%. Moreover, the α and γ angles of the AQ crystal changed, indicating that the AQ crystal underwent a distorted deformation following the Zn insertion. Prior to the Zn atom insertion, the intermolecular distance between the two AQ molecules was measured to be 3.91 Å (Figure 4a). Upon the insertion of a Zn atom into the AQ bulk, the intermolecular distance between the two AQ molecules bonded with the Zn atom decreased to 3.05 Å, while the intermolecular distance between the two AQ molecules not bonded with the Zn atom increased to 4.18 Å (Figure 4b). The intermolecular distance between the two AQ molecules bonded with the Zn atom is 21.99% smaller than the initial distance. The variation of the intermolecular distance of AQ is inseparable from the reduction in the AQ lattice constant. These results suggest that the insertion of Zn atoms causes significant structural instability in the AQ electrode, as evidenced by the alteration in the intermolecular distance between the two AQ molecules and the volume of the AQ supercell. This structural instability can lead to reduced capacity retention rates as the repeated insertion and de-insertion of Zn atoms into and out of the AQ electrode can further destabilize the crystal structure. Specifically, because the Zn ions have enough time to insert/de-insert from the surface to the inside of the AQ at a low current density, the reduplicative insertion/de-insertion processes in the charge–discharge cycles inevitably lead to the collapse of the AQ structure, resulting in rapid decreases in capacity. These discoveries explain that the capacity fading of AQ is more pronounced at a low current density energy from a crystallographic perspective.

Table 2. The relaxed lattice parameters of the AQ crystal before and after Zn insertion.

	a (Å)	**b (Å)**	**c (Å)**	**α (°)**	**β (°)**	**γ (°)**	**Volume (Å^3)**
AQ	15.63	11.75	15.66	90	102.29	90	2808.02
Zn inserted AQ	15.54	11.32	15.46	88.76	102.36	91.28	2654.74
Deformation (%)	−0.58	−3.66	−1.28	−1.38	0.07	1.42	−5.46

In order to understand the cyclic stability of the AQ electrode at a high and low current density, we utilized the climbing image nudged elastic band (CI-NEB) method to simulate the energy barrier of Zn inside the AQ bulk and on the AQ surface, respectively. We selected high-symmetry lines to identify favorable adsorption sites for the diffusion path. Figure 5a,c depicts the minimum energy path of the Zn diffusion inside the AQ bulk and on the AQ surface, respectively, with their corresponding energy barriers, as shown in Figure 5b,d. We investigated the possible spatial diffusion pathways of Zn between two adjacent adsorption sites. Consequently, there is only one possible diffusion pathway for Zn in the AQ bulk, which is illustrated in Figure 5a. This diffusion pathway is a curved path with a certain degree of curvature, and the energy barrier is as high as 3.185 eV, indicating that Zn atom migration in the AQ bulk is difficult. This high energy barrier should be ascribed to the steric hindrance caused by the H groups on the AQ molecule, and larger H groups may generate relatively more obstruction to the Zn diffusion. Furthermore, we also calculated the diffusion pathway and energy barrier of Zn on the AQ surface. The energy barrier was found to be only 0.171 eV, which is significantly lower than the energy barrier of Zn inside the AQ bulk. These results suggest that Zn atoms tend to diffuse on the AQ surface, which is another explanation for the observed larger cyclic capacity fading of AQ at a low current density. Although Zn atoms have sufficient time to insert into the interior of the AQ bulk from the AQ surface at a low current density, the energy barrier of Zn atoms in the AQ bulk is high, which limits the insertion and de-insertion of the Zn atoms during the charging and discharging process, resulting in a poor cyclic stability. Moreover, at a high current density, the charging and discharging time of Zn atoms is short, and they cannot be fully inserted in the interior of the AQ bulk. Therefore, the insertion/de-insertion process of Zn atoms can only take place on the AQ surface. The energy barrier of Zn atoms on the AQ surface was found to be only 0.171 eV, which facilitates the insertion and de-insertion of Zn ions during the charging and discharging process, leading to a good cyclic stability at a high current density. Our conclusions provide an explanation for the capacity fading of AQ at a low current density and the good capacity retention of AQ at a high current density.

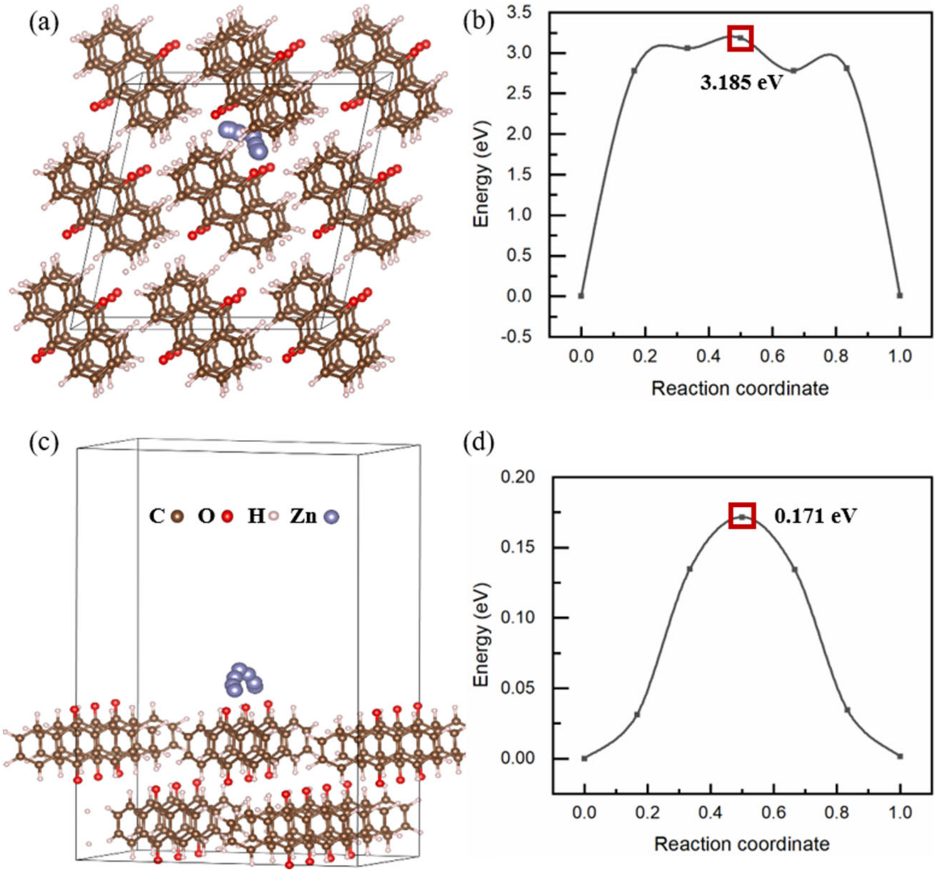

Figure 5. Schematic representations of Zn diffusion pathway (**a**) in AQ supercell and (**c**) on AQ surface; the corresponding energy barrier profiles of Zn (**b**) in AQ supercell and (**d**) on AQ surface. The red boxes indicate the maximum energy barriers during Zn diffusion process.

3. Materials and Methods

3.1. Electrode Preparation

To improve the conductivity of AQ, 0.7 g 9,10-anthraquinone (AQ) and 0.3 g Ketjen black (KB) were mixed uniformly via high energy ball milling (HEBM) at a rotation speed of 600 rpm for 5 h. After ball milling, the AQ/KB composite powder was obtained.

The prepared AQ/KB composite powder, super-P, and polytetrafluoroethylene (PTFE) were mixed homogeneously in a weight ratio of 70:15:15. AQ, KB, super-P, and PTFE were used as active material, conductive additives, and binder, respectively. Using isopropanol as solvent, this mixture was ground to a slurry. Then, the obtained slurry was manually pressed to a thin film with a thickness of 10–15 µm. This thin film was dried in vacuum at 60 °C overnight and then cut to small discs with a diameter of 12 mm. These small discs were pressed through a titanium mesh to prepare AQ electrode with an active material mass of 2–3 mg, corresponding to a mass load of 0.44–0.66 mg/cm^2.

3.2. Characterizations

The morphologies of the samples were characterized via transmission electron microscope (TEM, FEI Talos F200s). X-ray powder diffraction (XRD, Miniflex 600) patterns were carried out using Cu-Kα radiation (λ = 1.5406 Å) with a scan rate of 5° min^{-1} to demonstrate the structure of samples. Fourier transform infrared (FTIR) spectra were recorded using a FTIR spectrometer (Nicolet Is 50) in the wavelength range of 400–3000 cm^{-1}.

3.3. Electrochemical Measurements

To evaluate the electrochemical performance of the AQ/KB composite, 2032-type coin cells were assembled using AQ electrode as cathode, zinc foil as anode, 1M zinc sulfate

($ZnSO_4$) aqueous solution as the electrolyte, and Whatman glass fiber as separator in air, respectively. Galvanostatic charge/discharge (GCD) tests were characterized on a LAND battery system with potential range of 0.1–1.2 V. Cyclic voltammetry (CV) curves were measured on an electrochemical workstation (MULTI AUTOLAB M2004) using a scan rate of 0.1 mV/s from 0.2 to 1.0 V.

3.4. Computational Methods

First-principal calculations were performed using the Vienna ab-initio simulation package (VASP) code under the framework of DFT [28,29]. The electron exchange–correlation interactions were described using the generalized gradient approximation of Perdew, Burke, and Ernzerhof (PBE) [30], and the electron–ion interactions were treated using the projector-augmented wave (PAW) method. A plane wave kinetic energy cutoff of 500 eV was used. The van der Waals (vdW) correction is described by the density functional theory (DFT)-D3 method [31,32]. The convergence criteria for energy and force were 10^{-5} eV/atom and 0.01 eV/Å, respectively. The CI-NEB [33] method implemented in VASP was used to determine the diffusion energy barrier and the minimum energy pathways of Zn diffusion on the AQ bulk and surface.

The binding strength of the Zn adsorbate can be evaluated by calculating binding energy (E_{bind}) as follows:

$$E_{bind} = E_{X+Y} - E_X - E_Y, \tag{1}$$

where X, Y, and $X + Y$ represent the adsorbate, substrate, and adsorption system, respectively.

4. Conclusions

In this study, we investigated the cyclic stability of the AQ cathode in aqueous ZIBs through more than 1000 electrochemical cycles. Our discoveries indicate that the AQ electrode experiences a capacity fading rate of approximately 0.08% per cycle at a current density of 200 mA/g, while the fading rate decreases to around 0.03% per cycle at a higher current density of 4000 mA/g. Using the DFT calculations, we revealed that the process of Zn ions insertion/de-insertion in the AQ cathode results in a significant structure deformation of the AQ crystal, with the volume and intra-molecule distance change of 5.46% and 21.99%, respectively, indicating that the AQ electrode may undergo structural collapse after multiple charge–discharge cycles. We also used the Cl-NEB method to show that the energy barrier of Zn on the AQ surface is much lower (0.171 eV) than the energy barrier of Zn in the AQ bulk (3.185 eV), indicating that the Zn de-insertion from the AQ bulk is difficult. The insertion-induced structural deformation and irreversible Zn insertion into the AQ bulk can explain the obvious capacity fading of AQ at a low current density. In summary, our study provides valuable insights into the cyclic stability and diffusion behavior of the AQ cathode, which can be helpful in the development of advanced energy storage devices.

Author Contributions: Conceptualization, Q.C.; methodology, Q.C. and W.C.; software, Q.C. and W.C.; validation, Q.C. and W.C.; formal analysis, Q.C.; investigation, Q.C.; resources, D.S.; data curation, C.C.; writing—original draft preparation, Q.C. and X.L.; writing—review and editing, Q.C., X.L. and C.C.; supervision, D.S. and H.W.; project administration, D.S. and H.W.; funding acquisition, D.S. and C.C. All authors have read and agreed to the published version of the manuscript.

Funding: This work is supported by the National Natural Science Foundation of China (Grant No. 22109163 and 22209184) and the Xiamen Youth Innovation Fund (No. 3502Z20206081).

Data Availability Statement: Not applicable.

Conflicts of Interest: The authors declare no conflict of interest.

References

1. Fang, G.Z.; Zhou, J.; Pan, A.Q.; Liang, S.Q. Recent advances in aqueous zinc-ion batteries. *ACS Energy Lett.* **2018**, *3*, 2480–2501. [CrossRef]
2. Jia, X.X.; Liu, C.F.; Neale, Z.G.; Yang, J.H.; Cao, G.Z. Active materials for aqueous zinc ion batteries: Synthesis, crystal structure, morphology, and electrochemistry. *Chem. Rev.* **2020**, *120*, 7795–7866. [CrossRef] [PubMed]
3. Lin, X.D.; Zhou, G.D.; Robson, M.J.; Yu, J.; Kwok, S.C.T.; Ciucci, F. Hydrated deep eutectic electrolytes for high-performance zn-ion batteries capable of low-temperature operation. *Adv. Funct. Mater.* **2022**, *32*, 2109322. [CrossRef]
4. An, G.-H.; Hong, J.; Pak, S.; Cho, Y.; Lee, S.; Hou, B.; Cha, S. 2D metal zn nanostructure electrodes for high-performance zn ion supercapacitors. *Adv. Energy Mater.* **2020**, *10*, 1902981. [CrossRef]
5. Dunn, B.; Kamath, H.; Tarascon, J.-M. Electrical energy storage for the grid: A battery of choices. *Science* **2011**, *334*, 928–935. [CrossRef] [PubMed]
6. Wang, J.; Yang, Y.; Zhang, Y.; Li, Y.; Sun, R.; Wang, Z.; Wang, H. Strategies towards the challenges of zinc metal anode in rechargeable aqueous zinc ion batteries. *Energy Stor. Mater.* **2021**, *35*, 19–46. [CrossRef]
7. Kundu, D.; Adams, B.D.; Duffort, V.; Vajargah, S.H.; Nazar, L.F. A high-capacity and long-life aqueous rechargeable zinc battery using a metal oxide intercalation cathode. *Nat. Energy* **2016**, *1*, 16119. [CrossRef]
8. Gao, Y.J.; Li, G.F.; Wang, F.; Chu, J.; Yu, P.; Wang, B.S.; Zhan, H.; Song, Z.P. A high-performance aqueous rechargeable zinc battery based on organic cathode integrating quinone and pyrazine. *Energy Stor. Mater.* **2021**, *40*, 31–40. [CrossRef]
9. Zhu, T.T.; Zheng, K.; Wang, P.P.; Cai, X.; Wang, X.; Gao, D.M.; Yu, D.M.; Chen, C.G.; Liu, Y.P. A new zinc-ion battery cathode with high-performance: Loofah-like lanthanum manganese perovskite. *J. Colloid Interface Sci.* **2022**, *610*, 796–804. [CrossRef]
10. Yoo, G.; Koo, B.-R.; An, G.H. Nano-sized split V_2O_5 with H_2O-intercalated interfaces as a stable cathode for zinc ion batteries without an aging process. *Chem. Eng. J.* **2022**, *434*, 134738. [CrossRef]
11. Konarov, A.; Voronina, N.; Jo, J.H.; Bakenov, Z.; Sun, Y.-K.; Myung, S.-T. Present and future perspective on electrode materials for rechargeable zinc-ion batteries. *ACS Energy Lett.* **2018**, *3*, 2620–2640. [CrossRef]
12. Patil, N.; de la Cruz, C.; Ciurduc, D.; Mavrandonakis, A.; Palma, J.; Marcilla, R. An ultrahigh performance zinc-organic battery using poly(catechol) cathode in $zn(TFSI)_2$-based concentrated aqueous electrolytes. *Adv. Energy Mater.* **2021**, *11*, 2100939. [CrossRef]
13. Han, C.P.; Li, H.F.; Shi, R.Y.; Zhang, T.F.; Tong, J.; Li, J.Q.; Li, B.H. Organic quinones towards advanced electrochemical energy storage: Recent advances and challenges. *J. Mater. Chem. A* **2019**, *7*, 23378–23415. [CrossRef]
14. Miroshnikov, M.; Divya, K.P.; Babu, G.; Meiyazhagan, A.; Arava, L.M.R.; Ajayan, P.M.; John, G. Power from nature: Designing green battery materials from electroactive quinone derivatives and organic polymers. *J. Mater. Chem. A* **2016**, *4*, 12370–12386. [CrossRef]
15. Larcher, D.; Tarascon, J.M. Towards greener and more sustainable batteries for electrical energy storage. *Nat. Chem.* **2015**, *7*, 19–29. [CrossRef] [PubMed]
16. Zhao, Q.; Huang, W.; Luo, Z.; Liu, L.; Lu, Y.; Li, Y.; Li, L.; Hu, J.; Ma, H.; Chen, J. High-capacity aqueous zinc batteries using sustainable quinone electrodes. *Sci. Adv.* **2018**, *4*, eaao1761. [CrossRef]
17. Zhang, K.; Guo, C.Y.; Zhao, Q.; Niu, Z.Q.; Chen, J. High-performance organic lithium batteries with an ether-based electrolyte and 9,10-anthraquinone (AQ)/CMK-3 cathode. *Adv. Sci.* **2015**, *2*, 1500018. [CrossRef]
18. Guo, C.Y.; Zhang, K.; Zhao, Q.; Peia, L.K.; Chen, J. High-performance sodium batteries with the 9,10-anthraquinone/CMK-3 cathode and an ether-based electrolyte. *Chem. Commun.* **2015**, *51*, 10244–10247. [CrossRef]
19. Werner, D.; Apaydin, D.H.; Portenkirchner, E. An anthraquinone/carbon fiber composite as cathode material for rechargeable sodium-ion vatteries. *Batter. Supercaps* **2018**, *1*, 160–168. [CrossRef]
20. Zhang, Y.S.; Murtaza, I.; Liu, D.; Tan, R.; Zhu, Y.N.; Meng, H. Understanding the mechanism of improvement in practical specific capacity using halogen substituted anthraquinones as cathode materials in lithium batteries. *Electrochim. Acta* **2017**, *224*, 622–627. [CrossRef]
21. Wang, W.; Xu, W.; Cosimbescu, L.; Choi, D.W.; Li, L.Y.; Yang, Z.G. Anthraquinone with tailored structure for a nonaqueous metal-organic redox flow battery. *Chem. Commun.* **2012**, *48*, 6669–6671. [CrossRef] [PubMed]
22. Poizot, P.; Dolhem, F.; Gaubicher, J. Progress in all-organic rechargeable batteries using cationic and anionic configurations: Toward low-cost and greener storage solutions? *Curr. Opin. Electrochem.* **2018**, *9*, 70–80. [CrossRef]
23. Tomai, T.; Hyodo, H.; Komatsu, D.; Honma, I. Analysis of degradation mechanisms in quinone-based electrodes for aqueous electrolyte system via in situ XRD measurements. *J. Phys. Chem. C* **2018**, *122*, 2461–2466. [CrossRef]
24. Liang, Y.L.; Yao, Y. Positioning organic electrode materials in the battery landscape. *Joule* **2018**, *2*, 1690–1706. [CrossRef]
25. Phadke, S.; Cao, M.L.; Anouti, M. Approaches to electrolyte solvent selection for poly-anthraquinone sulfide organic electrode material. *ChemSusChem* **2018**, *11*, 965–974. [CrossRef] [PubMed]
26. Yan, L.J.; Zeng, X.M.; Li, Z.H.; Meng, X.J.; Wei, D.; Liu, T.F.; Ling, M.; Lin, Z.; Liang, C.D. An innovation: Dendrite free quinone paired with $ZnMn_2O_4$ for zinc ion storage. *Mater. Today Energy* **2019**, *13*, 323–330. [CrossRef]
27. Yan, L.J.; Zeng, X.M.; Zhao, S.; Jiang, W.; Li, Z.H.; Gao, X.H.; Liu, T.F.; Ji, Z.K.; Ma, T.L.; Ling, M.; et al. 9,10-Anthraquinone/$K_2CuFe(CN)_6$: A highly compatible aqueous aluminum-ion full-battery configuration. *ACS Appl. Mater. Interfaces* **2021**, *13*, 8353–8360. [CrossRef] [PubMed]

28. Kresse, G.; Hafner, J. Ab initio molecular-dynamics simulation of the liquid-metal–amorphous-semiconductor transition in germanium. *Phys. Rev. B* **1994**, *49*, 14251–14269. [CrossRef]
29. Kresse, G.; Furthmuller, J. Efficient iterative schemes for ab initio total-energy calculations using a plane-wave basis set. *Phys. Rev. B* **1996**, *54*, 11169–11186. [CrossRef]
30. Perdew, J.P.; Burke, K.; Ernzerhof, M. Generalized gradient approximation made simple. *Phys. Rev. Lett.* **1996**, *77*, 3865–3868. [CrossRef]
31. Grimme, S.; Antony, J.; Ehrlich, S.; Krieg, H. A consistent and accurate ab initio parametrization of density functional dispersion correction (DFT-D) for the 94 elements H-Pu. *J. Chem. Phys.* **2010**, *132*, 154104. [CrossRef] [PubMed]
32. Grimme, S.; Ehrlich, S.; Goerigk, L. Effect of the damping function in dispersion corrected density functional theory. *J. Comput. Chem.* **2011**, *32*, 1456–1465. [CrossRef] [PubMed]
33. Henkelman, G.; Uberuaga, B.P.; Jonsson, H. A climbing image nudged elastic band method for finding saddle points and minimum energy paths. *J. Chem. Phys.* **2000**, *113*, 9901–9904. [CrossRef]